PHYSICAL REVIEW RESEARCH **6**, 033342 (2024)

Orientation-resolved attosecond photoionization delays in the N_2O molecule

Celso M. González-Collado,[1] Laura Cattaneo,[2,3] Etienne Plésiat,[4] Juan J. Omiste,[5] Jannie Vos,[2]
Jesús González-Vázquez,[1,6] Piero Decleva,[7] Ursula Keller,[2] Alicia Palacios,[1,8] and Fernando Martín[1,4,*]
[1]*Departamento de Química, Módulo 13, Universidad Autónoma de Madrid, 28049 Madrid, Spain*
[2]*Physics Department, ETH Zurich, 8093 Zurich, Switzerland*
[3]*Max-Planck-Institut für Kernphysik, Saupfercheckweg 1, 69117 Heidelberg, Germany*
[4]*Instituto Madrileño de Estudios Avanzados en Nanociencia, Cantoblanco, 28049 Madrid, Spain*
[5]*Departamento de Química Física, Universidad Complutense de Madrid, 28040 Madrid, Spain*
[6]*Institute of Advanced Research in Chemical Sciences, Universidad Autónoma de Madrid, 28049 Madrid, Spain*
[7]*Dipartimento di Scienze Chimiche e Farmaceutiche, Università degli Studi di Trieste and CNR-IOM, 34127 Trieste, Italy*
[8]*Instituto de Física de la Materia Condensada, Universidad Autónoma de Madrid, 28049 Madrid, Spain*

(Received 11 April 2024; accepted 21 August 2024; published 27 September 2024)

We present a thorough theoretical and experimental investigation of photoionization time delays in the N_2O molecule. Our theory provides actual XUV+IR time-resolved photoelectron spectra as measured in real reconstruction of attosecond beating by interference of two-photon transitions (RABBIT) experiments. This requires not only accounting for the interaction between the XUV field and the neutral molecule, but also between the IR field and the ejected electron, which is only possible through explicit evaluation of a large number of dipole couplings between molecular electronic continuum states. To compare with the results of these calculations we have performed RABBIT experiments in which the ejected electron and the resulting ionic fragments are measured in coincidence, thus allowing us to obtain photoionization delays for a particular orientation of the molecule with respect to the polarization of the XUV and IR fields. We have found very good agreement between calculated and measured RABBIT spectra for both nondissociative and dissociative ionization channels. In particular, we unambiguously show a photoionization delay of about 60 as in the vicinity of a well-known shape resonance of N_2O in the nondissociative ionization channel. More importantly, we show a dramatic effect of the IR field in the orientation-resolved ionization delays in the whole photon energy range investigated in this paper (18–40 eV), even at the level of *relative* ionization delays (i.e., delays referred to an internal reference delay) where the effect of the IR field is generally assumed to cancel out. Finally, we explicitly show that the problem of spectral congestion inherent to most molecular systems, which usually prevents extraction of photoionization delays, is substantially alleviated by resolving the molecular orientation or, ideally, by resolving both the molecular orientation and the electron emission angle, where access to perfectly isolated ionization channels is possible at specific angles.

DOI: 10.1103/PhysRevResearch.6.033342

I. INTRODUCTION

Attosecond science has opened the way to access the natural time scale of electronic motion in atoms and molecules [1]. In this respect, attosecond pump-probe schemes, in which an XUV or x-ray attosecond pulse resulting from high-harmonic generation (HHG) or x-ray free electron lasers, respectively, is used to induce coherent electron dynamics that is subsequently probed by a second ultrashort pulse, have emerged as very promising tools to visualize and eventually control such dynamics [1–4]. In particular, streaking and interferometric methods in which single attosecond pulses and attosecond pulse trains (APTs) respectively overlap in time with a long femtosecond IR pulse have been used to retrieve photoionization delays [5–9]. These delays can be as short as a few tens of attoseconds depending on the system and the energy of the ionized electron. Among interferometric methods, probably the most popular one is reconstruction of attosecond beating by interference of two-photon transitions (RABBIT) [10,11]. In this method, a target gas is ionized in the presence of both an IR pulse and XUV APT, with a certain time delay between them, and the photoelectron spectrum is recorded as a function of the IR-XUV delay. Typically, the spectrum exhibits two types of bands, main bands or harmonic bands, which are due to the absorption of a single XUV photon and are therefore a replica of the XUV photoionization spectrum at the harmonic energies, and sidebands (SBs), which appear in between the main bands as a consequence of the additional absorption or emission of an IR photon. The two-photon paths involving the harmonic lying just above a given SB and the harmonic

---

[*] Contact author: fernando.martin@uam.es

lying just below it contribute to the same final state (i.e., the same SB), so that they interfere. Because of this, the amplitude of the SBs exhibits a periodic modulation with respect to the delay Δt between the XUV and the IR pulses, with a frequency equal to twice the IR frequency ω_{IR}:

$$S(\Delta t) = A + B\cos(2\omega_{\mathrm{IR}}\Delta t - \Delta\phi_{\mathrm{mol}} - \Delta\phi_{\mathrm{XUV}}). \quad (1)$$

When the phase difference given by the laser $\Delta\phi_{\mathrm{XUV}}$ (due to the attochirp) is known, Eq. (1) allows one to extract the intrinsic phase difference between the two interfering paths, $\Delta\phi_{\mathrm{mol}}$, and hence the two-photon ionization delay given by $\tau_{\mathrm{mol}} = \Delta\phi_{\mathrm{mol}}/2\omega_{\mathrm{IR}}$. RABBIT has been widely used to retrieve ionization time delays in atomic systems (see, e.g., Refs. [12–16] and references therein) and there is an increasing interest in applying it to molecules [17–25].

Two-photon ionization times resulting from the fit of the SBs to the above formula include the natural ionization time associated with absorption of the XUV photon, the so-called Wigner delay [26], and the effect of the probing with the IR field, which mainly interacts with the ejected electron and therefore leaves its signature in the measured ionization delay. In atoms, several approximate methods have been proposed and successfully applied [7], which allow one to approximately remove the effect of the IR pulse and, therefore, to access the intrinsic one-photon ionization delays. In molecules, the presence of the additional nuclear degrees of freedom, which are responsible for molecular vibrations and dissociation, further complicates this analysis. Indeed, as previous experimental and theoretical work in diatomic molecules has shown [19,21,23,25], the ionization times can significantly depend on how the excess photon energy is shared between electrons and nuclei. Furthermore, the multicentric nature of the potential felt by the escaping electron may also have a strong influence on the way the IR probe pulse interacts with the electron previously ionized by the XUV field [23], especially at low photoelectron energies, where most RABBIT experiments making use of APTs from HHG are performed. Finally, the proximity in energy of the different ionization channels inherent to most molecules usually leads to spectral congestion, in which harmonic bands and sidebands associated with different ionization channels overlap in the photoelectron spectra, often preventing one from extracting channel-resolved ionization delays. These complications are also inherent to any attosecond pump-probe experiment in molecules, not only RABBIT, so understanding them is crucial for the advancement of attosecond chemistry (or attochemistry), which seeks for new concepts and paradigms in chemistry [27,28].

A full understanding of the physics of ionization in molecules thus requires the support of accurate theoretical treatments in which both electronic and nuclear motions, as well as the coupling between them, are fully taken into account in a quantum mechanical way [29]. This has been shown to be especially important in the vicinity of narrow resonances [30], where ionization is significantly delayed with respect to nonresonant ionization, or at energies close to the ionization threshold, where the nuclei have enough time to move significantly before the electron can completely escape from the molecular potential. In addition, for a direct comparison with the experimental observable, the photoelectron spectrum, theory must not only account for the bound-continuum transitions induced by the XUV field, but also for continuum-continuum transitions induced by the IR field [31]. A complete theoretical description of RABBIT in molecules, including both electronic and nuclear degrees of freedom, has only been achieved for diatomics, where only one nuclear degree of freedom, the internuclear separation, is at play [19,30], and for CF_4 [23] and CH_4 [25] by reducing the number of nuclear degrees of freedom to just one.

In this paper we have considered the N_2O molecule, for which there exist some synchrotron radiation literature [32–35] and one of the earliest molecular RABBIT experiments [18]. *Relative* ionization delays reported in this early work were obtained by integrating over electron emission angle and for randomly oriented molecules. Theoretical calculations reported in that work have provided Wigner delays, i.e., delays obtained in the absence of the IR field. In the present paper, we have theoretically revisited RABBIT in N_2O and explicitly calculated RABBIT photoelectron spectra by including the effect of both the XUV and the IR fields. Due to the unaffordable computational cost of accounting for the four vibrational degrees of freedom in combination with the effect of the IR field, we have performed calculations in the fixed nuclei approximation (FNA). For obvious reasons, this approximation may fail for those channels where ionization is strongly coupled to nuclear motion, as, e.g., in the vicinity of Feshbach resonances or conical intersections, but is expected to provide a reliable description of nondissociative ionization channels, where the resulting N_2O^+ ion remains intact, or fully dissociative ionization channels that can univocally be associated to specific ionic fragments. To show that this is the case, we have performed RABBIT experiments where both electrons and ionic fragments, either intact N_2O^+ or smaller molecular cations, like N_2^+, NO^+, N^+, and O^+, have been detected in coincidence. The advantages of combining RABBIT with multicoincidence detection methods to study molecular systems has been highlighted in previous works [19,20,23,25,36,37]. The good agreement between theory and experiment for the nondissociative channel shows that one can rely on the FNA to interpret the origin of the measured delays in the nondissociative N_2O^+ channel and to quantify the role of the IR field in such delays without the use of any *ad hoc* model. Then, we have used this theory to obtain orientation- and/or angle-resolved information about photoionization delays. Our results confirm that, indeed, in this way, one can minimize the effect of the spectral congestion and retrieve ionization times for individual ionization channels. In particular, we show that the calculated photoionization delays for molecules oriented perpendicular to the polarization direction are in good agreement with the measured ones in most of the photon energy range covered by the present experiment. Surprisingly, we have found a dramatic effect of the IR field in the orientation-resolved ionization delays in the whole energy range investigated, even at the level of *relative* ionization delays where the effect of the IR is expected to approximately cancel out.

The paper is organized as follows. We first present the calculated photoionization delays and compare them with the present experimental results for the cases in which (i) neither the electron emission direction nor the molecular orientation

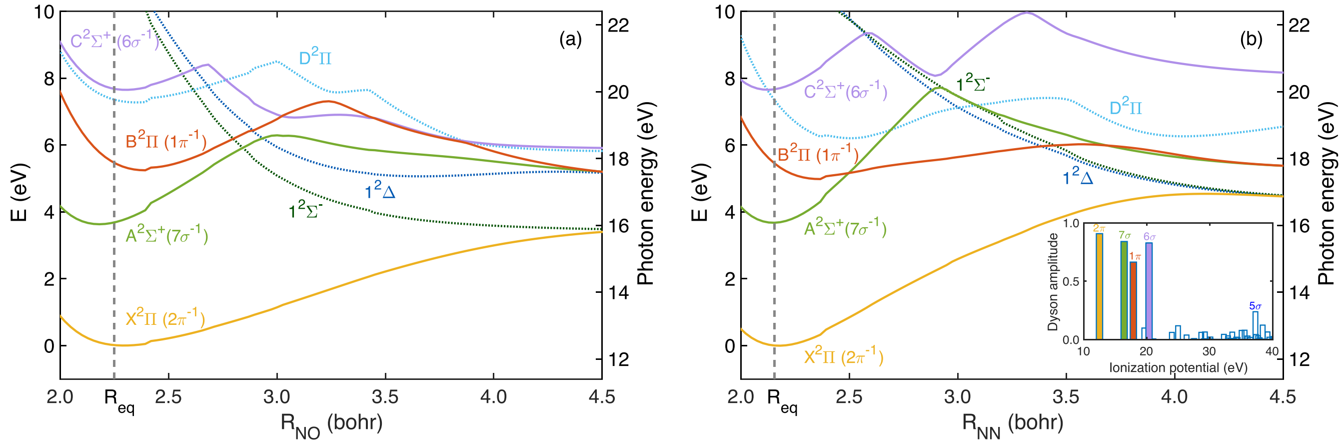

FIG. 1. Potential energy curves of N_2O^+ as a function of the NO distance (a) and the NN distance (b). The y axis on the left refers to the minimum of the potential energy surface in the ground state of the cation, $X^2\Pi$, while on the right it refers to the ground state of the neutral. The vertical dotted lines indicate the values of the NO and NN distances in the neutral molecule at the equilibrium geometry (see text). In both cases, the values of the frozen coordinates are those of the neutral molecule at the equilibrium geometry reported in Ref. [38]. The inset in panel (b) shows the squares of the Dyson norms for N_2O^+ states obtained at the geometry indicated by the dotted vertical line. Labels in the inset indicate the vacant orbital in the one-hole states.

is resolved and (ii) the molecular orientation is resolved. Then we present our theoretical predictions for orientation- and angle-resolved photoionization delays and discuss in detail how such measurements would allow one to identify ionization into specific channels. We conclude with a summary of the most important findings of the present paper.

II. POTENTIAL ENERGY SURFACES AND PHOTOIONIZATION CROSS SECTIONS

To clarify the relation between ionization channels and dissociative and nondissociative ionization paths in the photoionization of N_2O in the energy range considered in this paper, which is crucial for a proper comparison with the experimental results, we have calculated potential energy curves for several N_2O^+ states, as a function of (i) the NO distance with the NN distance fixed and (ii) the NN distance with the NO distance fixed. For the fixed distances, we have used the values for the neutral molecule at the equilibrium geometry reported by Rathbone *et al.* [38]: $R_{\text{eq,NO}} = 1.19$ Å and $R_{\text{eq,NN}} = 1.14$ Å. We have performed a state-averaged restricted active space self-consistent field (RASSCF) calculation with three inactive orbitals (1σ, 2σ, and 3σ), eight orbitals in RAS2, and six orbitals with a maximum of four electrons in RAS3: RASSCF(14,15). Our electronic states slightly improve on those previously reported by Chambaud *et al.* [39], who used a complete active space self-consistent field approach with full valence. The main difference is that we have included two extra π orbitals, which contribute to the NO bond and are, therefore, important to properly describe the dissociation limit and to perform a correct assignment of the states that are expected to contribute to the dissociative ionization channel. With the chosen basis, the calculated excitation energies at the equilibrium geometry are slightly higher than the experimental ones, however this basis provides a rather uniform accurate description over a wide range of internuclear distances. The results are shown in Fig. 1. As can be seen, the presence of several conical intersections makes it difficult to perform a one-to-one correspondence between a specific ionization channel and a specific dissociative ionization channel. However, it is rather clear that ionization leading to the $X^2\Pi$ and $A^2\Sigma^+$ states should lead almost exclusively to nondissociative ionization: the position of the minimum in the corresponding potential energy surfaces is similar to that of the ground state of the neutral molecule and the dissociation energy is of the order of 3 eV in both cases. Indeed, in a vertical transition from the ground state at the equilibrium geometry, represented by the vertical dashed line in Fig. 1, one can see that such line intersects the potential energy surface of the $A^2\Sigma^+$ $(7\sigma^{-1})$ state close to the minimum of the corresponding potential energy surface. This means that only the lowest vibrational states of the $A^2\Sigma^+$ $(7\sigma^{-1})$ state (v = 0, 1, 2,...) will be significantly populated due to the strong Franck-Condon overlap with the initial vibrational state of the neutral molecule ($v = 0$). As v increases in the $A^2\Sigma^+$ $(7\sigma^{-1})$ state, the overlap with the initial vibrational state decreases exponentially and becomes completely negligible above the dissociation limit. This is a well-known feature in molecular spectroscopy. In contrast, in Fig. 1(b), the vertical dashed line intersects the potential energy curve of the $B^2\Pi$ $(1\pi^{-1})$ state far from the minimum, in an energy region that lies very close to the dissociation limit. Taking into account that the $B^2\Pi$ $(1\pi^{-1})$ state is not exclusively populated at the intersection point between the dashed line and the corresponding potential energy curve, but in an energy region below and above this point, in many cases dissociation will effectively proceed without any barrier. As the probabilities to populate the $A^2\Sigma^+$ $(7\sigma^{-1})$ and $B^2\Pi$ $(1\pi^{-1})$ states (proportional to their corresponding cross sections shown in Fig. 2) are comparable in magnitude, one can safely conclude that most NO^+ + N dissociation will exclusively come from the $B^2\Pi$ $(1\pi^{-1})$ state.

Although evaluation of the electronic continuum states of N_2O at the same level of accuracy as the bound states of the N_2O^+ cation and inclusion of correlation between the ejected electron and the remaining ones can be done with

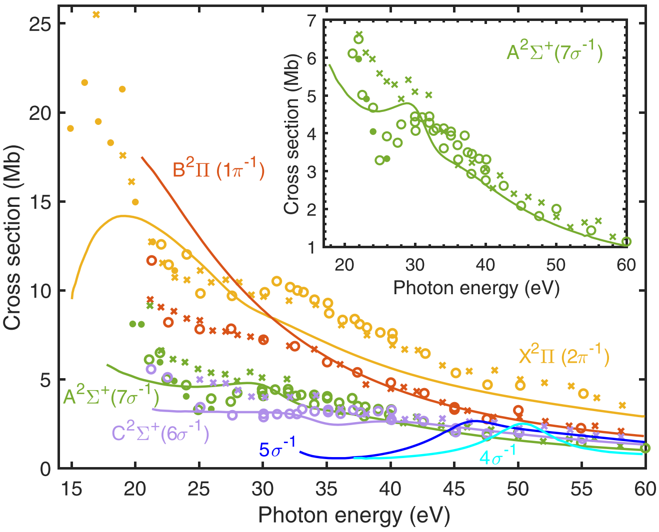

FIG. 2. Partial photoionization cross sections for randomly oriented N_2O molecules. Theory: full lines. Experiment: open and closed circles, Ref. [35]; crosses, Ref. [33]. No renormalization of the experimental data has been done. The ionization potential is 12.9 eV [46].

methods such as XCHEM [40,41], UK-Rmol+ [42,43], and others, this is impossible in the context of RABBIT due to the enormous computational cost associated with the need to perform a dense scan in XUV-IR delays. The static-exchange density-functional theory (DFT) method we have used in this paper (see Methods) is, in contrast, much cheaper but at the price of providing a poorer description of electron correlation. For instance, this method is only able to describe ionization leaving the remaining cation in a one-hole state. To check if this is a reasonable approximation in the present case, we have evaluated the Dyson amplitudes at the above-mentioned RASSCF level between the ground state of N_2O, which has N electrons, and the states of the corresponding cation, which has $N-1$ electrons, by using the usual formula

$$\varphi_k = \sqrt{N}\langle\Psi_k^{N-1}|\Psi^N\rangle. \tag{2}$$

The squares of the corresponding norms, $|\gamma_k|^2 = \langle\varphi_k|\varphi_k\rangle$, are related to the probability of ionization in the kth channel: if they are zero or very small, ionization in these channels will be negligible; if they are large, ionization will likely occur in these channels, although their relative importance cannot be guessed without evaluating the associated dipole transition matrix elements [44,45]. We have calculated the Dyson norms for several ionic states using the same state-averaged RASSCF(14,15) as above. The results depicted in the inset of Fig. 1 show that the larger Dyson norms are always associated with the one-hole states lying at the lower energies: $X^2\Pi$ $(2\pi^{-1})$, $A^2\Sigma^+$ $(7\sigma^{-1})$, $B^2\Pi$ $(1\pi^{-1})$, and $C^2\Sigma^+$ $(6\sigma^{-1})$. Among them, the $B^2\Pi$ $(1\pi^{-1})$ state is expected to be responsible for most of the NO^+ production because it is the only one-hole channel for which there is no barrier for breaking the NN bond [see Fig. 1(b)]. Therefore, one can expect that the static-exchange DFT method works reasonably well for this molecule. This conclusion is also supported by the good agreement between our calculated photoionization cross sections and those obtained in synchrotron radiation experiments [32,34] (see Fig. 2). Based on this result, we have calculated the RABBIT spectrum by assuming that the N_2O molecule can be ionized from four possible orbitals leading to the one-hole states $X^2\Pi$ $(2\pi^{-1})$, $A^2\Sigma^+$ $(7\sigma^{-1})$, $B^2\Pi$ $(1\pi^{-1})$, and $C^2\Sigma^+$ $(6\sigma^{-1})$.

Figure 2 includes a zoom of the $A^2\Sigma^+$ $(7\sigma^{-1})$ photoionization cross section in the shape resonance region, which will be the object of a detailed analysis in the following section. In the calculated cross sections, the maximum of the resonance peak appears at 28.8 eV, to be compared with 29.4 eV [33] and 30.8 eV [35] from the two existing synchrotron radiation experiments. The width of the peak extracted from the calculated cross section is approximately 8 eV, which is compatible with the values obtained from the experiments, approximately 5 eV [33] and 10 eV [35]. A detailed comparison with earlier theoretical calculations of the cross sections in this energy region [38,47] is given in the Supplemental Material [48].

III. RABBIT SPECTRA FOR RANDOMLY ORIENTED N_2O

In order to compare our results with those of the present experiment, the XUV and IR pulses were chosen to reproduce the experimental ones. Specifically, we have used an XUV APT whose harmonic comb is basically identical to the experimental one (see Fig. 1 in [48]). The APT has a global Gaussian envelope, 20-fs duration and peak intensity 5×10^{10} W/cm^2. The IR probe has the same Gaussian envelope, central frequency 1.59 eV, 20-fs duration, and peak intensity 5×10^{11} W/cm^2. In a few selected cases, we have checked that the calculated photoionization delays do not change significantly by reducing the intensity down to 1×10^{11} W/cm^2. For a meaningful comparison with experiment, in all RABBIT simulations, we have shifted the theoretical ionization potentials (IPs) to the experimental ones [49], since DFT is known to give an overall displacement of the states of the cation.

Figure 3 shows the calculated photoelectron spectrum obtained with the APT only [Fig. 3(a)], with both the APT and the IR pulses integrated over all APT-IR delays [Fig. 3(b)], the difference between the former two [Fig. 3(c)], and the photoelectron spectrum with both the APT and the IR pulses as a function of the APT-IR delay after subtraction of the XUV spectrum [Fig. 3(d)]. As can be seen, due to the proximity in energy of the different ionization channels, the main bands and the sidebands of several channels overlap with each other, making very difficult a correct assignment of all the observed features in a real experiment. Nevertheless, for those sidebands that are well isolated from other bands, one can see clear oscillations with the expected frequency $2\omega_{\mathrm{IR}}$, which would allow one to retrieve the ionization phases by using Eq. (1). Harmonic and sideband peaks below a photoelectron energy of 2 eV are nearly invisible.

As a result of the use of the fixed nuclei approximation in our calculations, for a meaningful comparison with the present experiment we will first consider nondissociative ionization channels. Figure 4 shows the measured time-of-flight spectra with the XUV APT only and with both the XUV APT and the IR pulse at zero delay. As can be seen, most of the signal

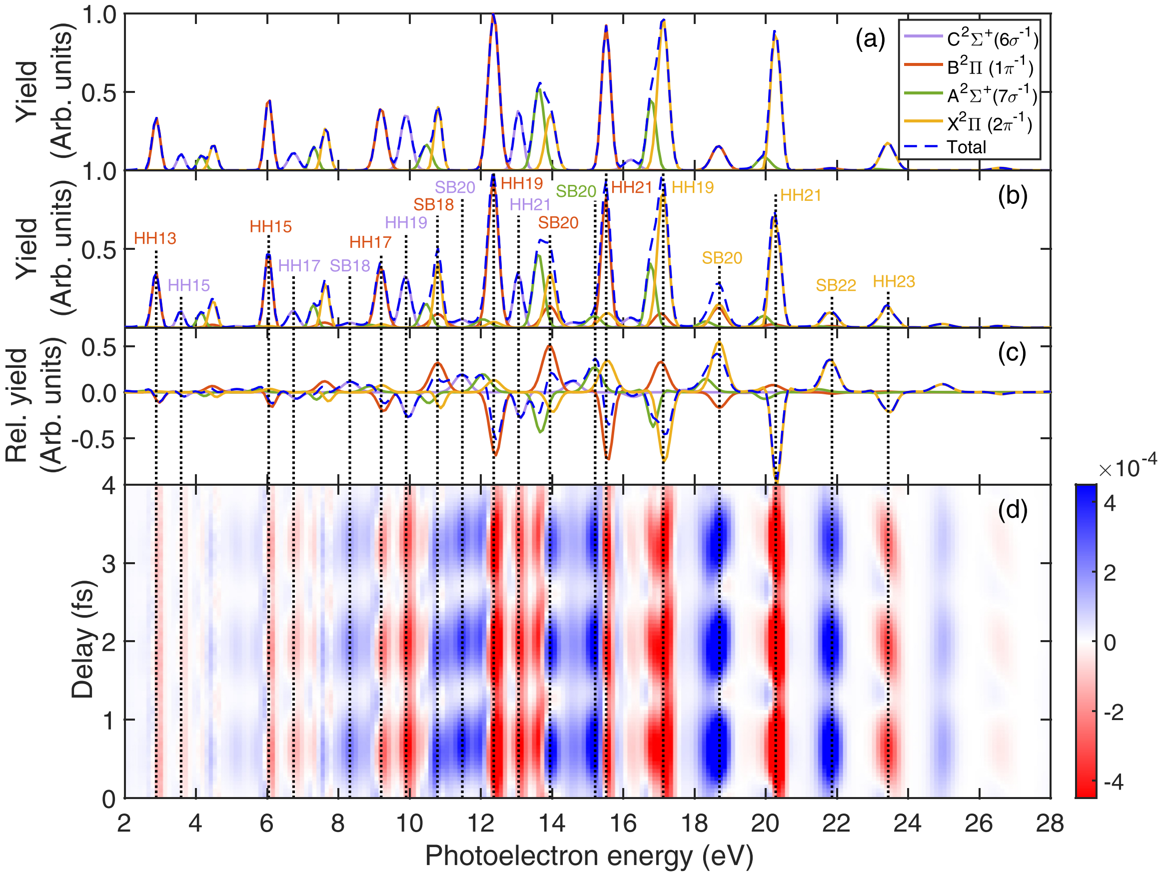

FIG. 3. (a) Calculated photoelectron spectrum obtained with the XUV APT only. (b) Calculated photoelectron spectrum obtained with both the XUV APT and the IR pulse integrated over all APT-IR delays. (c) Difference between the former two spectra. (d) Calculated photoelectron spectrum obtained with both the XUV APT and the IR pulse minus the XUV APT spectrum as a function of the APT-IR delay.

comes from the nondissociative path, i.e., N_2O^+ (note the logarithmic scale). As mentioned above, the channels leading to a molecular cation in the ground $X^2\Pi$ $(2\pi^{-1})$ and excited $A^2\Sigma^+$ $(7\sigma^{-1})$ states, following ionization from the 2π highest occupied molecular orbital (HOMO) and 7σ HOMO-1 orbitals, respectively, are expected to be the most important contributors to the nondissociative process in the investigated energy range. So, in Fig. 5, we have compared the calculated RABBIT spectrum for the sum of the $X^2\Pi$ $(2\pi^{-1})$ and $A^2\Sigma^+$ $(7\sigma^{-1})$ channels [Fig. 5(b)] with the experimental one for the nondissociative ionization signal [Fig. 5(a)]. A more quantitative comparison is provided by the difference between the APT-only and APT+IR spectra integrated over all delays [Fig. 5(c)], since such difference highlights the contribution of the sidebands, which are the ones containing the information about the ionization phases. The agreement is good. This means that time delays extracted from the calculated spectra can be used for further physical analysis.

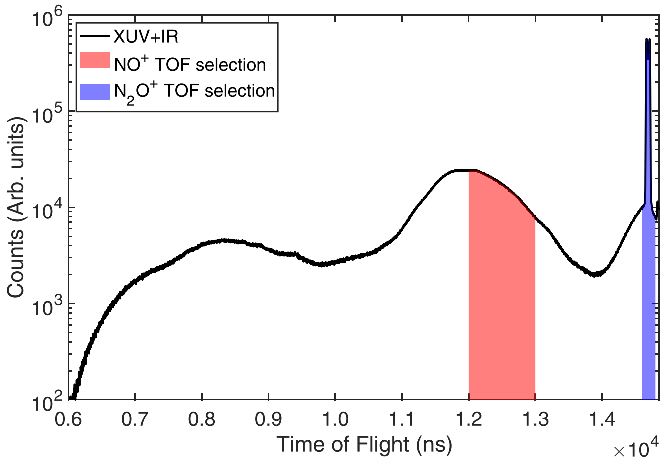

FIG. 4. Time of flight with highlighted sections corresponding to different fragments.

In Fig. 5(d) we have plotted the photoionization delays extracted from the calculated sidebands associated with the nondissociative $X^2\Pi$ $(2\pi^{-1})$ and $A^2\Sigma^+$ $(7\sigma^{-1})$ channels over the whole range of photoelectron energies. As can be seen, the calculated delays are negative [except for SB18 and SB20 in the $A^2\Sigma^+$ $(7\sigma^{-1})$ channel], indicating that the electrons escape more rapidly in the presence of the molecular potential than if they were free. At first sight, this may seem counterintuitive, but one should not forget that the extracted delays correspond to two-photon ionization and thus include the effect of the interaction of the IR field with the ionized electron, which in this case leads to an acceleration of the electron (see below). For the $X^2\Pi$ $(2\pi^{-1})$ channel, the photoionization delay monotonically increases from approximately −40 to −20 as in the investigated energy range, while for the $A^2\Sigma^+$ $(7\sigma^{-1})$

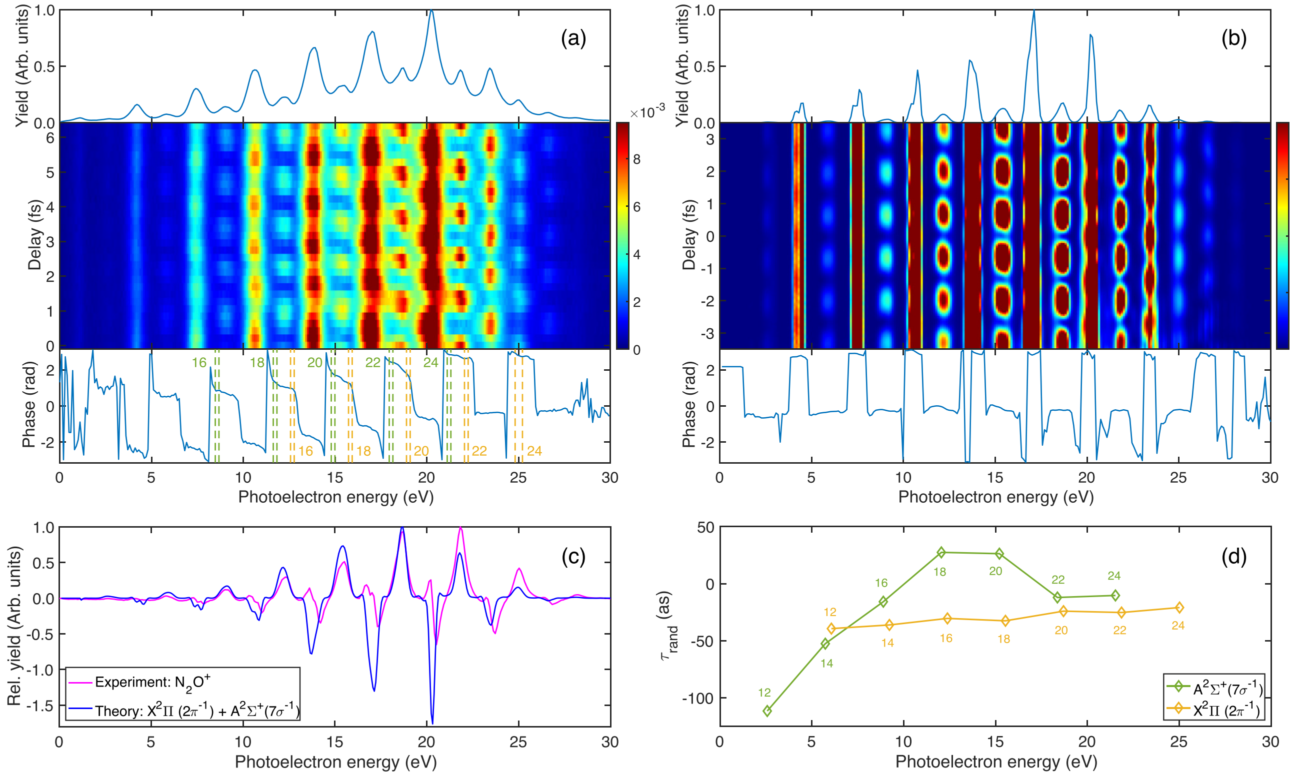

FIG. 5. (a) Experimental RABBIT spectrum for nondissociative ionization of N_2O (central panel). Upper panel: RABBIT spectrum integrated over XUV-IR delay. Lower panel: Phases extracted from the Fourier transform of the RABBIT spectrum. Labels indicate sideband orders. Vertical dashed lines indicate the energy intervals used to extract the photoionization delays. The separation between the extraction areas is larger than that between the maxima of the sideband peaks for the $X^2\Pi$ $(2\pi^{-1})$ and $A^2\Sigma^+$ $(7\sigma^{-1})$ channels to avoid contamination between each other in the chosen areas. (b) Theoretical RABBIT spectrum of N_2O corresponding to the sum of the $X^2\Pi$ $(2\pi^{-1})$ and $A^2\Sigma^+$ $(7\sigma^{-1})$ channels. Notations are as in (a). (c) Comparison between theoretical and experimental delay-integrated spectra. For the sake of clarity, the XUV-only spectrum has been subtracted. (d) Theoretical delays extracted from the individual $X^2\Pi$ $(2\pi^{-1})$ and $A^2\Sigma^+$ $(7\sigma^{-1})$ contributions to the spectrum shown in (b).

channel, it rapidly increases at the lower photoelectron energies, then reaches a maximum at around 12–15 eV, and then decreases at higher energies. This abrupt variation of the photoionization delay is due to the presence of a well-known shape resonance in the $A^2\Sigma^+$ $(7\sigma^{-1})$ ionization channel at ≈ 28-eV photon energy (see Fig. 2).

For the nondissociative channel, a direct comparison of the absolute delays shown in Fig. 5(d) with experiment is not possible because in order to do so one should remove the effect of the APT attochirp from the measurements. As the attochirp is usually not known, the usual way out is to consider an internal reference and provide *relative* ionization delays instead of absolute ones, so that this unknown quantity cancels out. Due to the spectral overlap between different channels in molecules, this is not always easy to do in practice. However, in the present case, since only the $X^2\Pi$ $(2\pi^{-1})$ and $A^2\Sigma^+$ $(7\sigma^{-1})$ channels contribute to the nondissociative spectrum, their individual contributions to the spectrum can be reasonably extracted. As can be seen in Fig. 5(a), around a photoelectron energy of ≈ 18 eV, the SB20 and SB22, associated with, respectively, the $X^2\Pi$ $(2\pi^{-1})$ and $A^2\Sigma^+$ $(7\sigma^{-1})$ channels, nearly overlap, leading to a broad oscillatory band with a rather complex structure. In particular, in the borders of such band one can distinguish two different phases in the oscillations, each one corresponding to one of the two channels. The same can be observed around 15 eV for the corresponding SB18 and SB20 bands, and around 12 eV for the corresponding SB16 and SB18 bands. This is confirmed by the presence of two narrow plateaus in the Fourier transforms, separated by a slowly decreasing phase in the region where the respective SBs overlap [see bottom panel of Fig. 5(a)]. At higher energies, the SBs are exclusively associated to the $X^2\Pi$ $(2\pi^{-1})$ channel, so identification is straightforward. Extraction of the corresponding phases from theory is easy since one has access to the separate contributions to the RABBIT spectrum from each individual channel.

Figure 6 shows the calculated relative ionization delays between the $X^2\Pi$ $(2\pi^{-1})$ and $A^2\Sigma^+$ $(7\sigma^{-1})$ channels as a function of photon energy, which are compared with the corresponding relative Wigner delays and the present experimental results. One can see a maximum of the ionization delay at around 28 eV, which is due to the presence of the shape resonance in the *A* channel. The shape resonance leads to an increase of the ionization time in the *A* channel, which does not occur in the *X* channel [see the flatness of the *X* ionization delay in Fig. 5(d)]. Therefore, if one assumes that the effect of the IR field is the same in the two channels, one can roughly estimate the lifetime of the shape resonance in the *A* state, which according to this figure is ≈ 60 as, in good agreement with the value extracted from the width of the peak observed

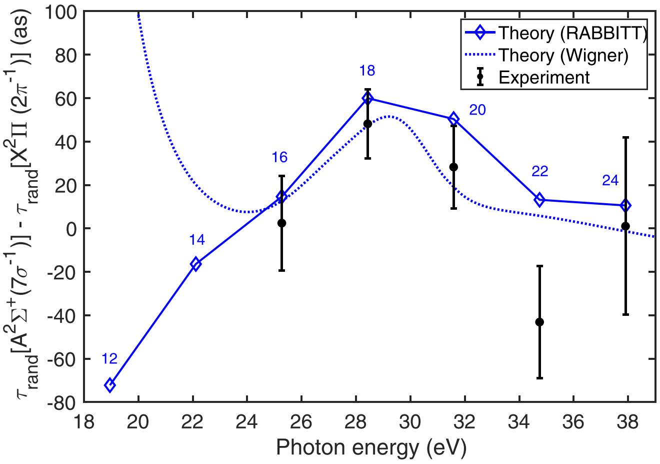

FIG. 6. Relative photoionization delays between the $X^2\Pi(2\pi^{-1})$ and $A^2\Sigma^+(7\sigma^{-1})$ channels. Blue rhombus: present theoretical results. Black circles: present experimental results from the average over three different runs; the bars indicate the statistical error. Dotted blue curve: relative Wigner delays.

in the synchrotron radiation spectrum at around 28 eV for this channel (see Fig. 2).

This analysis is supported by the fact that the general trend of the relative one-photon Wigner delays is similar to that of the full calculation or the experiment at photon energies above 25 eV. Nevertheless, the former are systematically lower (by as much as 30 as at around 32 eV) than those directly extracted from the sidebands. At photon energies below 25 eV, i.e., below the shape resonance, the relative Wigner delays also fail in describing the variation of the two-photon delays with photoelectron energy. In fact, as can be seen, in this region the contribution of the IR field to the measured photoionization delay is much larger than the one-photon Wigner delay. The rapid change of the relative two-photon delays in this low-energy region mainly reflects the rapid evolution of the difference of the absolute molecular phases with photoelectron energy as one approaches the ionization threshold. The large discrepancy with the Wigner results suggests that the continuum-continuum phases introduced by the IR field vary similarly or even more rapidly near threshold. These results show that, even though one might have expected the effect of the IR field to be the same in both channels and hence to cancel out in the relative delays, this is not the case irrespective of the fact that the difference in photoelectron energy between the absolute delays at a given photon energy is only 3.5 eV. Therefore, in order to compare with experimental measurements, one should incorporate the effect of the IR field in the ionization process, even at the level of relative delays. This conclusion goes along the same spirit as that reported in [50] based on a simple model.

To disentangle the different contributions in the spectrum of Fig. 3, we have explored two different strategies. One requires orientation of the molecule and the other one electron-ion coincidence detection. In either scenario, we have first considered several molecular orientations to separate different channels by electron energy (or, equivalently, sideband order). Then, we have studied the relevant channels at different emission angles of the ejected electron, in addition to molecular orientation. Each strategy has its own advantages and disadvantages from the experimental point of view, as we will discuss throughout the rest of the paper. For instance, the first one provides better statistics, as one does not need to resolve the electron emission angle. In contrast, the second one has the potential to provide the most complete information about individual channels and the molecular landscape [23].

IV. RABBIT SPECTRA FOR ORIENTED N_2O

We first consider an experimental scenario in which neither the electron emission angle is resolved nor the atomic and molecular ions resulting from ionization are detected. We assume, however, that the experiment can resolve the molecular orientation, even for the nondissociative channel.

We define the orientation of the molecule as the angle β between the molecular axis and the polarization direction of the laser pulses, which is the same for both XUV and IR. For simplicity, we have considered two cases: the parallel orientation ($\beta = 0^\circ$) and the perpendicular orientation ($\beta = 90^\circ$). To begin with, in the RABBIT spectrum for the parallel case [see Fig. 7(a)] we only have contributions from the $C^2\Sigma^+$ $(6\sigma^{-1})$, $A^2\Sigma^+$ $(7\sigma^{-1})$, and $X^2\Pi$ $(2\pi^{-1})$ channels, but the $B^2\Pi$ $(1\pi^{-1})$ is not present at all, as expected from the photoionization cross sections for this particular orientation (see Fig. 2 in [48]). This is already a simpler scenario than in Fig. 3 for the case of random orientation. Furthermore, the sidebands of these three channels appear at different electron energies. Thus it is possible to isolate the time delay of the $C^2\Sigma^+$ $(6\sigma^{-1})$ and $A^2\Sigma^+$ $(7\sigma^{-1})$ channels, on the one hand, and the $X^2\Pi$ $(2\pi^{-1})$ channel, on the other hand, just by looking at the sidebands at the electron energies where they are dominant. Figure 7(c) shows a comparison between ionization delays extracted from the total spectrum (i.e., including the contribution from all channels) and those extracted separately from each individual channel. As can be seen, delays extracted from the total spectrum at around 5 eV, where the $C^2\Sigma^+$ $(6\sigma^{-1})$ and $A^2\Sigma^+$ $(7\sigma^{-1})$ channels dominate, are similar to the individual delays in these particular channels, while delays extracted from the total spectrum at around 22 eV, where the $X^2\Pi$ $(2\pi^{-1})$ channel dominates, basically correspond to delays in the $X^2\Pi$ $(2\pi^{-1})$ channel. It is worth mentioning that the time delay changes significantly at around 15 eV of photoelectron energy as a consequence of the shape resonance mentioned above [50]. In this region, the three channels have a significant contribution to the total spectrum, so that delays extracted from this spectrum do not correspond to any of the delays of the individual channels.

In the perpendicular case, we have a similar situation but now the main contributions to the RABBIT spectrum come from the $B^2\Pi$ $(1\pi^{-1})$ and $X^2\Pi$ $(2\pi^{-1})$ channels, as we can see in Fig. 7(b) (see also the one-photon ionization cross sections in Fig. 2 in [48]). Also, the variation of the delays with electron energy is much smaller [see Fig. 7(d)], due to the smoother variation of the cross sections (see Fig. 2 and Fig. 2 in [48]). At lower energies the delays extracted from the total spectrum reflect those in the $B^2\Pi$ $(1\pi^{-1})$ channel, while at higher energies they reflect those in the $X^2\Pi$ $(2\pi^{-1})$ channel. We note that the differences in the time delays between the

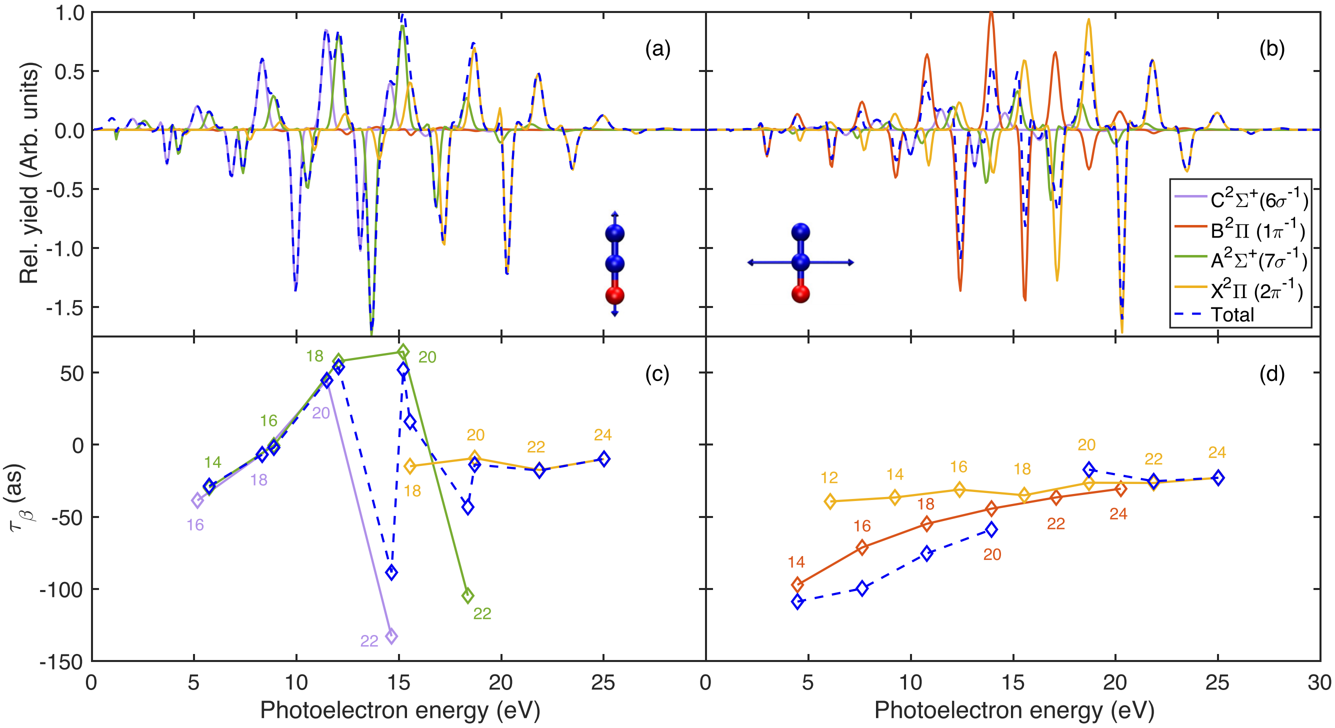

FIG. 7. Spectrum resulting after integration of the RABBIT spectrum over all XUV-IR delays and subtraction of the XUV-only spectrum for (a) parallel and (b) perpendicular orientation. The separate contribution of the individual channels is also shown. (c) Time delays extracted from the spectrum shown in (a) with indication of the sideband orders. (d) Same as (c) from the spectrum shown in (b). In (d) we do not provide the delay extracted from the total spectrum at around 17 eV because this is the region where the very intense HH19 band for the X channel fully overlaps with the weak SB22 band for the B channel.

parallel and perpendicular orientations reflect the anisotropy of the molecular potential due to its multicentric nature.

When the molecular orientation is determined by measuring in coincidence photoelectrons and fragment ions, as in the present experiment, one only has access to the dissociative ionization channel. As discussed above (see Fig. 1), dissociative ionization leading to NO^+ fragments should almost exclusively proceed through the $B^2\Pi\ (1\pi^{-1})$ channel. This is because, in a vertical transition describing ionization from the ground state at the equilibrium geometry, this is the only channel leading to dissociation into $NO^+ + N$ [the $D^2\Pi$ state lying at slightly higher energy, which can also dissociate in the same way, is barely populated by ionization because it is not a one-hole state; see the corresponding small Dyson norm in the inset of Fig. 1(b)]. As mentioned above, in this channel, dissociative ionization is expected to be comparable in magnitude to or even dominate over nondissociative ionization. The fixed-nuclei approximation has been shown to provide accurate photoionization cross sections when dissociative ionization is the dominant ionization process, as, e.g., in the CF_4 molecule, where the resulting ground-state molecular cation CF_4^+ fully dissociates. This has also been shown to be the case for CF_4 in the context of RABBIT, even at the level of electron angular distributions (see, e.g., [23]). Thus, we have compared our calculated RABBIT spectra for the $B^2\Pi\ (1\pi^{-1})$ channel with the experimental one obtained by measuring the photoelectron and the NO^+ fragment in coincidence, both of them for $\beta = 90^\circ$. The experimental and calculated spectra are shown in Figs. 8(a) and 8(b), and the retrieved photoionization delays, referred to the delays of the nondissociative channel $X^2\Pi\ (2\pi^{-1})$, are shown in Fig. 9. As can be seen, the agreement between theory and experiment is good, thus showing that coincidence measurements indeed allow one to isolate individual channels. A similar comparison with experiment at $\beta = 0^\circ$ is not possible due to the lower statistics. Figure 9 also shows the calculated Wigner delays for the $B^2\Pi\ (1\pi^{-1})$ channel referred to the Wigner delays in the nondissociative channel $X^2\Pi\ (2\pi^{-1})$. As can be seen, except at the higher photon energies, the one-photon Wigner delays do not agree with the actual delays extracted from the RABBIT spectra. In fact, the Wigner delays are always positive, while the latter are always negative.

V. RABBIT SPECTRA FOR ORIENTED N_2O WITH ANGULAR RESOLUTION

We consider now the experimental scenario in which both the photoelectron emission direction and the molecular orientation can be determined, but without detection of the ionic fragments. This is possible, e.g., by orienting the molecule with a laser. We have calculated the spectra for both parallel and perpendicular orientations of the molecule and for each photoionization channel. Then, we have integrated over the time delays between the pulses, the azimuthal angle of the emitted electron (ϕ), and around each sideband (±0.6 eV). We have also integrated over a cone of $\beta = \pm 30^\circ$ to account for the hypothetical experimental error, as such cone would be necessary to obtain enough statistics for angular resolution.

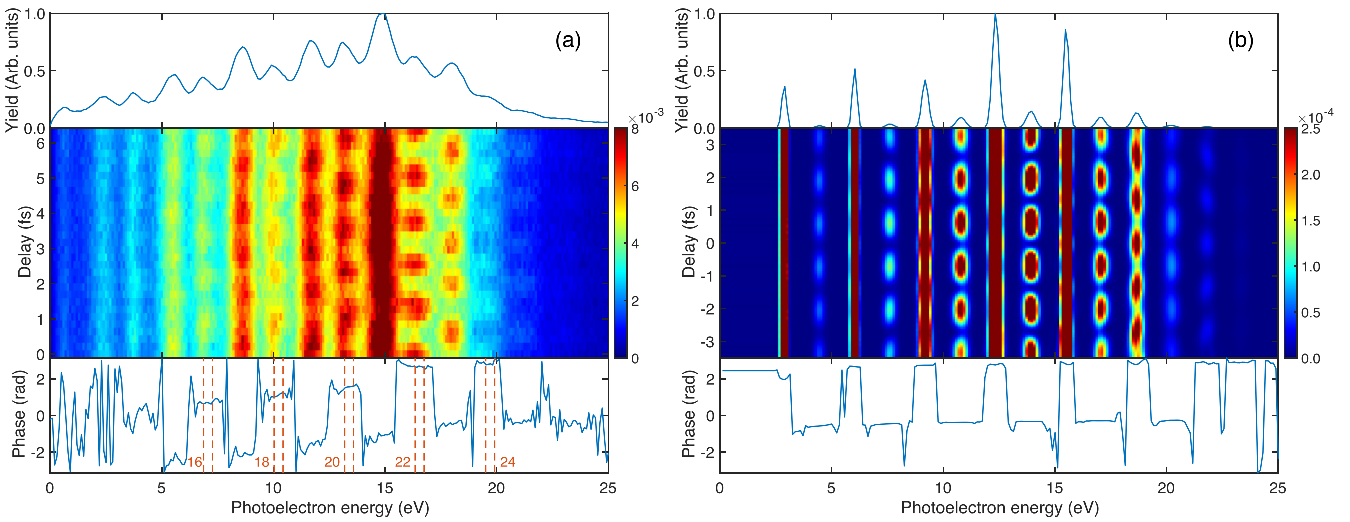

FIG. 8. (a) Experimental RABBIT spectrum of N_2O molecules oriented perpendicular to the polarization direction leading to NO^+ fragments (central panel). Upper panel: spectrum integrated over XUV-IR delay. Lower panel: Phases extracted from the Fourier transform of the RABBIT spectrum. Labels indicate sideband orders. Vertical dashed lines indicate the energy intervals used to extract the photoionization delays. (b) Theoretical RABBIT spectrum for the $B^2\Pi$ $(1\pi^{-1})$ channel at $\beta = 90^\circ$. Notations are as in (a).

Figure 10 shows the resulting spectra as a function of the polar angle of the emitted electron (θ) for several sidebands, for both parallel [Figs. 10(a) and 10(c)] and perpendicular [Figs. 10(b) and 10(d)] orientations. We can see that the emission angle θ has a strong effect on the amplitude of the spectra, which show a clear anisotropy for all channels. For instance, we can see that in every case the amplitudes of all channels go to almost zero around the emission directions perpendicular to the lasers, i.e., $\theta = 90^\circ$ when $\beta \approx 0^\circ$ and $\theta = 0^\circ, 180^\circ$ when $\beta \approx 90^\circ$. It is also important to highlight the fact that in some cases there are only significant contributions from one or two relevant channels. For example, when $\beta \approx 0^\circ$, the θ ranges $[0–10]^\circ$ and $[170–180]^\circ$ are dominated by the $C^2\Sigma^+$ $(6\sigma^{-1})$ and $A^2\Sigma^+$ $(7\sigma^{-1})$ channels for most of the sidebands [see Fig. 10(a)]. This is of course related to what we have already discussed in the previous section [Fig. 7(a)] but now we can get rid of the $X^2\Pi$ $(2\pi^{-1})$ contribution too by selecting the mentioned angular ranges. However, the most striking result is that for $\beta \approx 90^\circ$ and $\theta = [80–100]^\circ$ the only relevant contribution comes from the $B^2\Pi$ $(1\pi^{-1})$ channel for all sidebands [see Fig. 10(b)], proving that this channel can be completely isolated at specific angles.

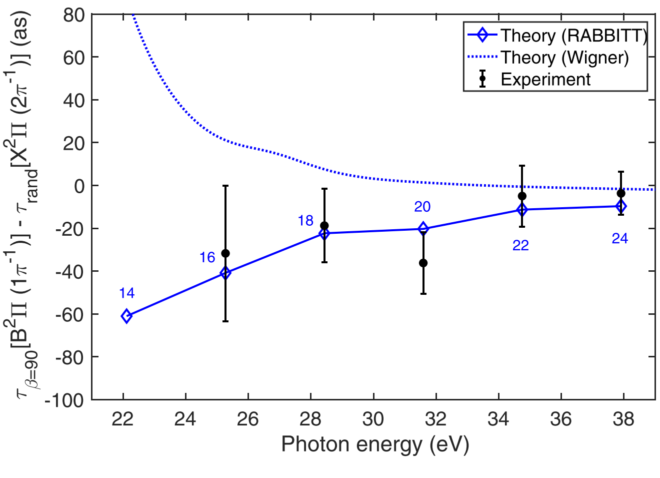

FIG. 9. Experimental (circles) and theoretical (rhombus) photoionization delays extracted from the spectra shown in Figs. 8(a) and 8(b), respectively, referred to the delays of the nondissociative channel $X^2\Pi$ $(2\pi^{-1})$ extracted from Figs. 5(a) and 5(b), respectively. The experimental values result from the average over three different runs; the bars indicate the statistical error. Labels indicate sideband orders. Dotted blue curve: Wigner delays for the $B^2\Pi$ $(1\pi^{-1})$ channel at $\beta = 90^\circ$ refer to those in the $X^2\Pi$ $(2\pi^{-1})$ channel for randomly oriented molecules.

Figure 11 shows the calculated two-photon delays as a function of electron emission angle for the parallel and the perpendicular orientations. For comparison, the corresponding one-photon Wigner delays are also shown. As can be seen, the two-photon delays are extremely sensitive to both electron emission direction and orientation, and so are the Wigner delays. However, the latter barely catch the actual variations of the two-photon delays with these parameters. In particular, the Wigner delays have very often the opposite sign to the two-photon delays. Both kinds of delays show the pronounced anisotropy of the molecular potential that holds the shape resonance, in agreement with the results of recent RABBIT experiments on CF_4 in which electrons and ions were detected in coincidence [23].

VI. CONCLUSIONS

We have performed a detailed theoretical investigation of photoionization delays in the N_2O molecule by simulating actual RABBIT spectra as measured in real experiments. This requires accounting for the interaction between the XUV field and the molecule, but also between the ejected electron and the IR field, which has a significant effect in the measured delays. Due to computational limitations, calculations have been performed within the fixed nuclei approximation, which restricts comparison with experiment to the nondissociative

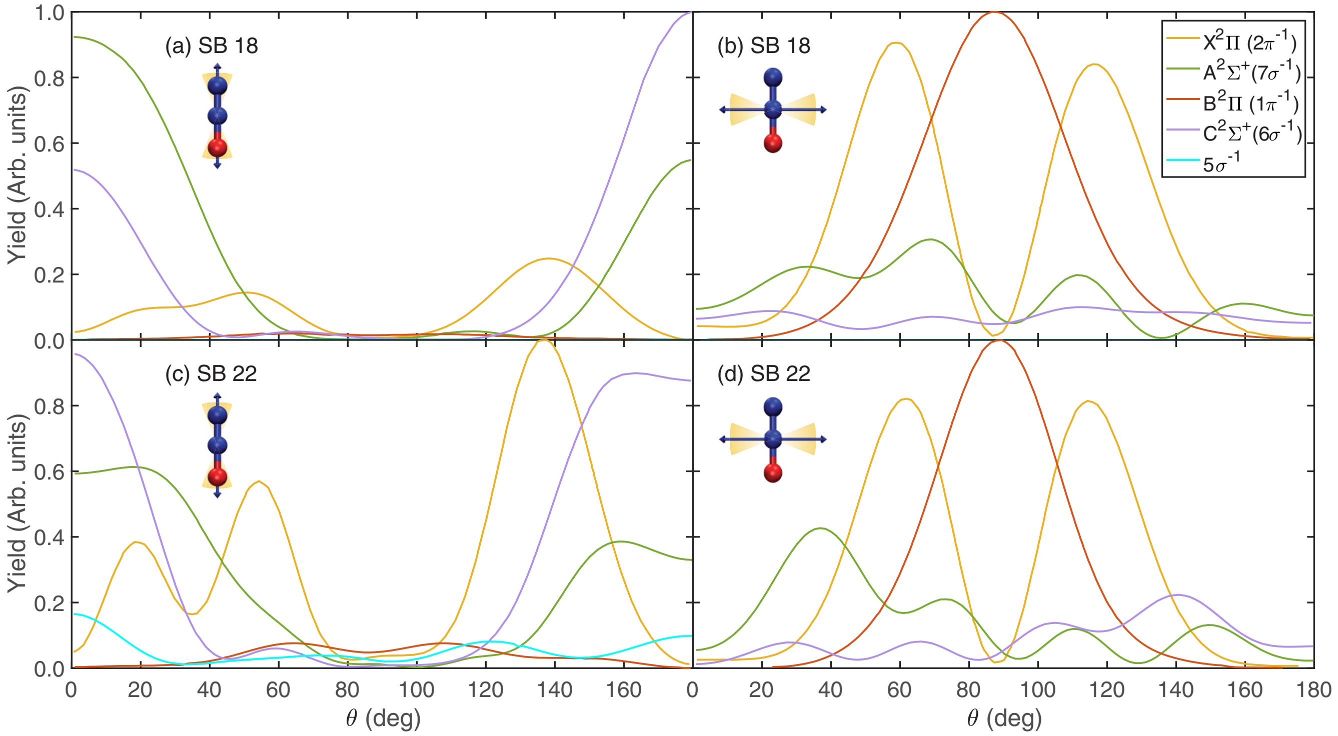

FIG. 10. Fully differential photoelectron spectra around SB18 and SB22 after integration of the RABBIT spectrum over all XUV-IR delays and subtraction of the XUV-only spectrum for (a), (c) $\beta = 0 \pm 30^\circ$ (parallel orientation) and (b), (d) $\beta = 90 \pm 30^\circ$ (perpendicular orientation), as a function of the photoelectron emission polar angle (see text).

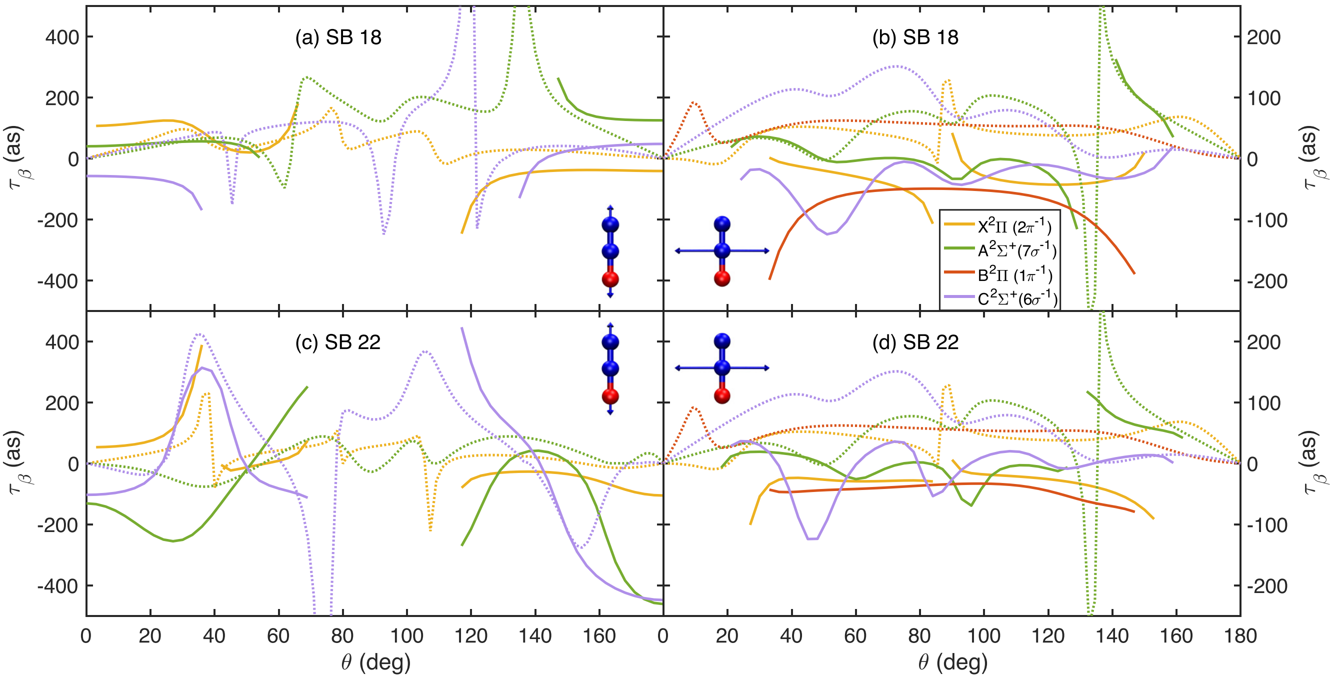

FIG. 11. Differential two-photon (full lines) and Wigner (dotted lines) delays around SB18 and SB22 for (a), (c) $\beta = 0^\circ$ (parallel orientation) and (b), (d) $\beta = 90^\circ$ (perpendicular orientation), as a function of the photoelectron emission polar angle (see text). All delays have been integrated over the photoelectron azimuthal angle. Two-photon delays have not been extracted in those angular regions where the photoionization cross section is nearly zero (see Fig. 10).

ionization channels leading to a bound N_2O^+ molecular ion or to the dissociative channel leading to NO^+ fragments. To compare with the results of these calculations we have performed RABBIT experiments in which not only the ejected electron but also the produced ionic fragments are measured in coincidence, thus allowing us to select the desired nondissociative and dissociative ionization channels. We have found very good agreement between calculated and measured RABBIT spectra for the nondissociative channel, showing the appropriateness of the theoretical treatment in describing the interaction of the molecule with the two fields. Then we have gone a step further and shown that the problem of spectral congestion due to the proximity in energy of the different ionization channels, which usually prevents extraction of photoionization delays from experiment, can be substantially reduced by resolving the molecular orientation or even better by resolving both the molecular orientation and the electron emission angle, totally or partially. Ultimately, this procedure may allow one to extract ionization delays for individual channels, as shown here for dissociative ionization leading to NO^+ fragments when the molecule is oriented perpendicular to the polarization direction or as suggested by recent RABBIT experiments performed in CF_4 [23] (which dissociates with 100% efficiency after ionization). Importantly, we have shown that ignoring the effect of the IR field can have dramatic consequences in the interpretation of the measured photoionization delays. A similar finding has recently been reported for the H_2^+ molecular ion [51]. Combining RABBIT with multicoincidence detection methods or laser induced orientation is nowadays possible.

As shown in this paper, this can help resolving spectral congestion in molecular systems, which is one of the main challenges in current RABBIT experiments. In N_2O, the cylindrical symmetry helps by effectively reducing the number of ionization channels at given molecular orientations. This is expected to be the case for larger molecules exhibiting some kind of symmetry, although the larger number of accessible ionization channels may complicate the analysis. In the absence of any symmetry, resolving molecular orientation may not be significantly more advantageous than standard RABBIT experiments in which molecular orientation is not resolved. For such molecules, relying on theoretical methods as the one presented in this paper, which can be easily applied to molecules containing up to a few tens of atoms, is probably the most convenient approach. Another alternative to minimize the problem of spectral congestion would be the use of shorter wavelengths, so that harmonic bands and sidebands are further apart. We hope that the present paper will thus spur future experimental work in this direction, knowing that theory is now ready to provide actual observables for this kind of molecules, i.e., photoelectron spectra that can be directly compared with experiment.

VII. METHODS

A. Theory

The theoretical method has been discussed in detail elsewhere [9], so here we will only provide a brief summary. To describe the electronic structure of N_2O and its ionization continuum at the equilibrium geometry [38], we have used the multicenter B-spline static-exchange DFT method [31,52–56]. Within this framework, we described the bound states with DFT, using the LB94 functional, and we included all the continuum states below the energy cutoff of 40.8 eV. Following common practice, we have performed a close-coupling expansion of the electronic continuum wave function in terms of partial waves with well-defined angular momentum of the continuum electron. The proper asymptotic conditions of these continuum states have been imposed by means of the so-called Galerkin approach [57]. For the one-center expansion of the wave functions, we included partial waves with angular momentum up to $L_{\max} = 18$ and a basis of 1400 B-splines defined in a box of 810 a.u. For the off-center expansions around each atomic site, we included angular momenta up to 3 and B-splines within a box of 0.4 a.u. From the calculated electronic wave functions, we have evaluated bound-bound, bound-continuum, and continuum-continuum dipole couplings (in the length gauge) as described in [9]. Electronic energies, wave functions, and dipole couplings were then used to solve the time-dependent Schrödinger equation [Eq. (3)]

$$i\frac{\partial}{\partial t}\,\Phi(\boldsymbol{r},t) = [H^0 + V(t)]\,\Phi(\boldsymbol{r},t) \tag{3}$$

in the framework of the spectral method and in an all-electron treatment as described in Ref. [9]. This equation has been repeatedly solved in a grid of 161 delays between the XUV APT and the IR pulse to obtain the corresponding RABBIT spectrum. As mentioned above, in all calculations we have considered that the geometry of the molecule does not change with time. We have considered all one-hole electronic states accessible by the XUV: $X^2\Pi$ $(2\pi^{-1})$, $A^2\Sigma^+$ $(7\sigma^{-1})$, $B^2\Pi$ $(1\pi^{-1})$, and $C^2\Sigma^+$ $(6\sigma^{-1})$, shifting their ionization potentials to the experimental ones [49]. Once the above equation has been solved and the wave function has been obtained at sufficiently long times, a given observable, e.g., a photoelectron spectrum associated with a particular ionization channel, is obtained by projecting this wave function onto the asymptotic state associated with such observable.

B. Experiment

The XUV pulses were generated by focusing a strong, linearly polarized IR field (central wavelength 785 nm) into an argon gas target, which results in an APT centered at 35 eV, which only comprises odd multiples of the fundamental IR frequency ω_{IR}. We use a COLTRIMS detector [58,59] with an attosecond front end [60] to measure electrons and ions after XUV photon absorption in the 20–45-eV range. We focused the XUV pump beam onto a cold jet (backing pressure ≈2.5 bars) of N_2O molecules. A replica of the photon spectrum is created in the photoelectron spectrum at energy of the high harmonics minus the IP for the N_2O^+ ions or the dissociation limit when the molecules break up and both nuclear and electron kinetic energy are considered. At the spatial and temporal overlap of the XUV pump beam with the IR probe beam (estimated peak intensity $\approx 10^{11}$ W/cm^2 and pulse duration ≈30 fs) two-photon transitions are induced. As mentioned above, such a signal appears in the photoelectron spectrum as an oscillating SB signal as the delay Δt between the pump and probe beam is scanned. Each RABBIT trace is collected for all (fragment) ions and integrated over the complete kinetic energy range and all angles of the ionic and electronic parts of the reaction. We only consider those photoelectrons emitted within a cone with opening angle $\alpha = \pm 60^\circ$ with respect to the laser polarization axis. We integrate the spectrum for 3600 s (repetition rate 10 kHz) at each delay point (spaced by $\approx$0.2 fs). The NO$^+$ fragment-ion selection has been performed solely considering the time of flight between 12 000 and 13 000 ns. The experimental results of the relative photoionization time delays were obtained after averaging over three independent runs measured on different days and the error bars correspond to the standard deviation of those runs.

ACKNOWLEDGMENTS

This paper is based upon work from COST Action CA18222 (AttoChem), supported by COST (European Cooperation in Science and Technology), and has been supported by Projects No. PID2022-138288NB-C31, No. PID2022-138288NB-C32, No. PID2022-138288NB-C33 and No. PID2021-122839NB-I00 funded by MCIN/AEI Grant No. 10.13039/501100011033/FEDER UE, the “Severo Ochoa” Programme for Centres of Excellence in Research and Development (Grant No. CEX2020-001039-S), and the “María de Maeztu” Programme for Units of Excellence in Research and Development (Grant No. CEX2018-000805-M). All calculations were performed at the Mare Nostrum Supercomputer of the Red Española de Supercomputación and the Centro de Computación Científica de la Universidad Autónoma de Madrid. The experimental work at ETH Zurich was partially supported by NCCR Molecular Ultrafast Science and Technology, a research instrument of the Swiss National Science Foundation (SNSF), and by SNSF Project No. 200020-200416. L.C. acknowledges the Max Planck Group Leader program for funding her independent research. J.J.O. acknowledges funding by the Madrid Government (Comunidad de Madrid Spain) under the Multiannual Agreement with Universidad Complutense de Madrid in the Line Research Incentive for Young PhDs, in the context of V PRICIT (Regional Programme of Research and Technological Innovation) Grant No. PR27/21-010.

[1] F. Krausz and M. Ivanov, Attosecond physics, Rev. Mod. Phys. **81**, 163 (2009).

[2] M. Drescher, M. Hentschel, R. Kienberger, M. Uiberacker, V. Yakovlev, A. Scrinzi, T. Westerwalbesloh, U. Kleineberg, U. Heinzmann, and F. Krausz, Time-resolved atomic inner-shell spectroscopy, Nature (London) **419**, 803 (2002).

[3] G. Sansone, F. Kelkensberg, J. F. Perez-Torres, F. Morales, M. F. Kling, W. Siu, O. Ghafur, P. Johnsson, M. Swoboda, E. Benedetti *et al.*, Electron localization following attosecond molecular photoionization, Nature (London) **465**, 763 (2010).

[4] F. Calegari, D. Ayuso, A. Trabattoni, L. Belshaw, S. De Camillis, S. Anumula, F. Frassetto, L. Poletto, A. Palacios, P. Decleva, J. B. Greenwood *et al.*, Ultrafast electron dynamics in phenylalanine initiated by attosecond pulses, Science **346**, 336 (2014).

[5] J. Itatani, F. Quéré, G. L. Yudin, M. Y. Ivanov, F. Krausz, and P. B. Corkum, Attosecond streak camera, Phys. Rev. Lett. **88**, 173903 (2002).

[6] E. Goulielmakis, M. Uiberacker, R. Kienberger, A. Baltuska, V. Yakovlev, A. Scrinzi, T. Westerwalbesloh, U. Kleineberg, U. Heinzmann, M. Drescher *et al.*, Direct measurement of light waves, Science **305**, 1267 (2004).

[7] J. M. Dahlström, D. Guénot, K. Klünder, M. Gisselbrecht, J. Mauritsson, A. L’Huillier, A. Maquet, and R. Taïeb, Theory of attosecond delays in laser-assisted photoionization, Chem. Phys. **414**, 53 (2013).

[8] Á. Jiménez-Galán, F. Martín, and L. Argenti, Two-photon finite-pulse model for resonant transitions in attosecond experiments, Phys. Rev. A **93**, 023429 (2016).

[9] E. Plésiat, M. Lara-Astiaso, P. Decleva, A. Palacios, and F. Martín, Real-time imaging of ultrafast charge dynamics in tetrafluoromethane from attosecond pump-probe photoelectron spectroscopy, Chem. Eur. J. **24**, 12061 (2018).

[10] P.-M. Paul, E. S. Toma, P. Breger, G. Mullot, F. Augé, P. Balcou, H. G. Muller, and P. Agostini, Observation of a train of attosecond pulses from high harmonic generation, Science **292**, 1689 (2001).

[11] R. López-Martens, K. Varjú, P. Johnsson, J. Mauritsson, Y. Mairesse, P. Salières, M. B. Gaarde, K. J. Schafer, A. Persson, S. Svanberg *et al.*, Amplitude and phase control of attosecond light pulses, Phys. Rev. Lett. **94**, 033001 (2005).

[12] M. Schultze, M. Fieß, N. Karpowicz, J. Gagnon, M. Korbman, M. Hofstetter, S. Neppl, A. L. Cavalieri, Y. Komninos, T. Mercouris *et al.*, Delay in photoemission, Science **328**, 1658 (2010).

[13] K. Klünder, J. M. Dahlström, M. Gisselbrecht, T. Fordell, M. Swoboda, D. Guénot, P. Johnsson, J. Caillat, J. Mauritsson, A. Maquet *et al.*, Probing single-photon ionization on the attosecond time scale, Phys. Rev. Lett. **106**, 143002 (2011).

[14] M. Kotur, D. Guénot, Á Jiménez-Galán, D. Kroon, E. W. Larsen, M. Louisy, S. Bengtsson, M. Miranda, J. Mauritsson, C. L. Arnold, S. E. Canton, M. Gisselbrecht, T. Carette, J. M. Dahlström, E. Lindroth, A. Maquet, L. Argenti, F. Martín, and A. L’Huillier, Spectral phase measurement of a fano resonance using tunable attosecond pulses, Nat. Commun. **7**, 10566 (2016).

[15] V. Gruson, L. Barreau, Á. Jiménez-Galan, F. Risoud, J. Caillat, A. Maquet, B. Carré, F. Lepetit, J.-F. Hergott, T. Ruchon, L. Argenti, R. Taïeb, F. Martín, and P. Salières, Attosecond dynamics through a fano resonance: Monitoring the birth of a photoelectron, Science **354**, 734 (2016).

[16] C. Cirelli, C. Marante, S. Heuser, C. L. M. Petersson, Á. J. Galán, L. Argenti, S. Zhong, D. Busto, M. Isinger, S. Nandi, S. Maclot, L. Rading, P. Johnsson, M. Gisselbrecht, M. Lucchini, L. Gallmann, J. M. Dahlström, E. Lindroth, A. L’Huillier, F. Martín, and U. Keller, Anisotropic photoemission time delays close to a fano resonance, Nat. Commun. **9**, 955 (2018).

[17] S. Haessler, B. Fabre, J. Higuet, J. Caillat, T. Ruchon, P. Breger, B. Carré, E. Constant, A. Maquet, E. Mével *et al.*, Phase-resolved attosecond near-threshold photoionization of molecular nitrogen, Phys. Rev. A **80**, 011404(R) (2009).

[18] M. Huppert, I. Jordan, D. Baykusheva, A. von Conta, and H. J. Wörner, Attosecond delays in molecular photoionization, Phys. Rev. Lett. **117**, 093001 (2016).

[19] L. Cattaneo, J. Vos, R. Y. Bello, A. Palacios, S. Heuser, L. Pedrelli, M. Lucchini, C. Cirelli, F. Martín, and U. Keller, Attosecond coupled electron and nuclear dynamics in dissociative ionization of H_2, Nat. Phys. **14**, 733 (2018).

[20] J. Vos, L. Cattaneo, S. Patchkovskii, T. Zimmermann, C. Cirelli, M. Lucchini, A. Kheifets, A. S. Landsman, and U. Keller, Orientation-dependent stereo wigner time delay and electron localization in a small molecule, Science **360**, 1326 (2018).

[21] S. Nandi, E. Plésiat, S. Zhong, A. Palacios, D. Busto, M. Isinger, L. Neoričić, C. L. Arnold, R. J. Squibb, R. Feifel, P. Decleva, A. L'Huillier, F. Martín, and M. Gisselbrecht, Attosecond timing of electron emission from a molecular shape resonance, Sci. Adv. **6**, eaba7762 (2020).

[22] I. Jordan, M. Huppert, D. Rattenbacher, M. Peper, D. Jelovina, C. Perry, A. von Conta, A. Schild, and H. J. Wörner, Attosecond spectroscopy of liquid water, Science **369**, 974 (2020).

[23] H. Ahmadi, E. Plésiat, M. Moioli, F. Frassetto, L. Poletto, P. Decleva, C. D. Schröter, T. Pfeifer, R. Moshammer, A. Palacios, F. Martín, and G. Sansone, Attosecond photoionisation time delays reveal the anisotropy of the molecular potential in the recoil frame, Nat. Commun. **13**, 1242 (2022).

[24] X. Gong, S. Heck, D. Jelovina, C. Perry, K. Zinchenko, R. Lucchese, and H. J. Wörner, Attosecond spectroscopy of size-resolved water clusters, Nature (London) **609**, 507 (2022).

[25] X. Gong, É. Plésiat, A. Palacios, S. Heck, F. Martín, and H. J. Wörner, Attosecond delays between dissociative and non-dissociative ionization of polyatomic molecules, Nat. Commun. **14**, 4402 (2023).

[26] E. P. Wigner, Lower limit for the energy derivative of the scattering phase shift, Phys. Rev. **98**, 145 (1955).

[27] M. Nisoli, P. Decleva, F. Calegari, A. Palacios, and F. Martín, Attosecond electron dynamics in molecules, Chem. Rev. **117**, 10760 (2017).

[28] F. Calegari and F. Martín, Open questions in attochemistry, Commun. Chem. **6**, 184 (2023).

[29] F. Martín, Ionization and dissociation using B-splines: Photoionization of the hydrogen molecule, J. Phys. B **32**, R197 (1999).

[30] V. J. Borràs, J. González-Vázquez, L. Argenti, and F. Martín, Attosecond photoionization delays in the vicinity of molecular feshbach resonances, Sci. Adv. **9**, eade3855 (2023).

[31] A. Palacios and F. Martín, The quantum chemistry of attosecond molecular science, WIREs Comput. Mol. Sci. **10**, e1430 (2020).

[32] U. Gelius, Recent progress in esca studies of gases, J. Electron Spectrosc. Relat. Phenom. **5**, 985 (1974).

[33] C. E. Brion and K. H. Tan, Partial oscillator strengths for the photoionization of N_2O and CO_2 (20–60 eV), Chem. Phys. **34**, 141 (1978).

[34] W. Domcke, L. S. Cederbaum, J. Schirmer, W. Von Niessen, C. E. Brion, and K. H. Tan, Experimental and theoretical investigation of the complete valence shell ionization spectra of CO_2 and N_2O, Chem. Phys. **40**, 171 (1979).

[35] T. A. Carlson, P. R. Keller, J. W. Taylor, T. Whitley, and F. A. Grimm, Angle-resolved photoelectron spectroscopy of N_2O measured as a function of photon energy from 14 to 70 eV, J. Chem. Phys. **79**, 97 (1983).

[36] D. Ertel, D. Busto, I. Makos, M. Schmoll, J. Benda, H. Ahmadi, M. Moioli, F. Frassetto, L. Poletto, C. D. Schröter, T. Pfeifer, R. Moshammer, Z. Mašín, S. Patchkovskii, and G. Sansone, Influence of nuclear dynamics on molecular attosecond photoelectron interferometry, Sci. Adv. **9**, eadh7747 (2023).

[37] D. Ertel, D. Busto, I. Makos, M. Schmoll, J. Benda, F. Bragheri, R. Osellame, E. Lindroth, S. Patchkovskii, Z. Mašín, and G. Sansone, Anisotropy parameters for two-color photoionization phases in randomly oriented molecules: Theory and experiment in methane and deuteromethane, J. Phys. Chem. A **128**, 1685 (2024).

[38] G. J. Rathbone, E. D. Poliakoff, J. D. Bozek, D. Toffoli, and R. R. Lucchese, Photoelectron trapping in $N_2O\,7\sigma \rightarrow k\sigma$ resoxsnant ionization, J. Chem. Phys. **123**, 014307 (2005).

[39] G. Chambaud, H. Gritli, P. Rosmus, H.-J. Werner, and P. J. Knowles, The ion-molecule reaction $O^+\,(^4S) + N_2(X^1\sigma^+) \rightarrow NO^+(X^1\sigma^+, \nu') + N(^4S)$ and the predissociation of the $A^2\sigma^+$ and $B^2\pi$ states of N_2O^+, Mol. Phys. **98**, 1793 (2000).

[40] C. Marante, L. Argenti, and F. Martín, Hybrid GaussianB-spline basis for the electronic continuum: Photoionization of atomic hydrogen, Phys. Rev. A **90**, 012506 (2014).

[41] C. Marante, M. Klinker, I. Corral, J. González-Vázquez, L. Argenti, and F. Martín, Hybrid-basis close-coupling interface to quantum chemistry packages for the treatment of ionization problems, J. Chem. Theory Comput. **13**, 499 (2017).

[42] L. R. Moore, M. A. Lysaght, L. A. A. Nikolopoulos, J. S. Parker, H. W. van der Hart, and K. T. Taylor, The RMT method for many-electron atomic systems in intense short-pulse laser light, J. Mod. Opt. **58**, 1132 (2011).

[43] J. M. Carr, P. G. Galiatsatos, J. D. Gorfinkiel, A. G. Harvey, M. A. Lysaght, D. Madden, Z. Mašín, M. Plummer, J. Tennyson, and H. N. Varambhia, UKRmol: A low-energy electron- and positron-molecule scattering suite, Eur. Phys. J. D **66**, 58 (2012).

[44] V. Pomogaev, S. Lee, S. Shaik, M. Filatov, and C. H. Choi, Exploring Dyson's orbitals and their electron binding energies for conceptualizing excited states from response methodology, J. Phys. Chem. Lett. **12**, 9963 (2021).

[45] J. V. Ortiz, Dyson-orbital concepts for description of electrons in molecules, J. Chem. Phys. **153**, 070902 (2020).

[46] K. Kimura, *Handbook of HeI Photoelectron Spectra of Fundamental Organic Molecules: Ionization Energies, Ab Initio Assignments, and Valence Electronic Structure for 200 Molecules* (Halsted, New York, 1981).

[47] M. Braunstein and V. McKoy, Shape resonances in the photoionization of N_2O, J. Chem. Phys. **87**, 224 (1987).

[48] See Supplemental Material at http://link.aps.org/supplemental/10.1103/PhysRevResearch.6.033342 for further details of the theoretical calculations and the angular selection performed in the experiment.

[49] M. Lebech, J. C. Houver, D. Dowek, and R. R. Lucchese, Dissociative photoionization of N_2O in the region of the $N_2O^+(B\ ^2\pi)$ state studied by ion–electron velocity vector correlation, J. Chem. Phys. **120**, 8226 (2004).

[50] D. Baykusheva and H. J. Wörner, Theory of attosecond delays in molecular photoionization, J. Chem. Phys. **146**, 124306 (2017).

[51] A. J. Suñer Rubio, C. Lemell, R. Y. Bello, J. Burgdörfer, A. Palacios, and F. Martín, Attosecond photoionization delays in molecules: The role of nuclear motion, Phys. Rev. Res. **6**, L022066 (2024).

[52] M. Stener, G. Fronzoni, D. Toffoli, and P. Decleva, Time dependent density functional photoionization of CH_4, NH_3, H_2O and HF, Chem. Phys. **282**, 337 (2002).

[53] M. Stener, P. Decleva, I. Cacelli, R. Moccia, and R. Montuoro, Response function study of co photoionization: Ab initio SCF and density functional results, Chem. Phys. **272**, 15 (2001).

[54] M. Stener, G. Alti, and P. Decleva, Convergence of the density functional one-centre expansion for the molecular continuum: N2 and (CH3)3N, Theor. Chim. Acta **101**, 247 (1999).

[55] M. Stener and P. Decleva, Time-dependent density functional calculations of molecular photoionization cross sections: N_2 and PH_3, J. Chem. Phys. **112**, 10871 (2000).

[56] M. Stener, G. Fronzoni, and P. Decleva, Time dependent density functional study of the symmetry resolved N 1s photoionization in N_2, Chem. Phys. Lett. **351**, 469 (2002).

[57] D. Toffoli, M. Stener, G. Fronzoni, and P. Decleva, Convergence of the multicenter B-spline DFT approach for the continuum, Chem. Phys. **276**, 25 (2002).

[58] R. Dörner, V. Mergel, O. Jagutzki, L. Spielberger, J. Ullrich, R. Moshammer, and H. Schmidt-Böcking, Cold target recoil ion momentum spectroscopy: A “momentum microscope” to view atomic collision dynamics, Phys. Rep. **330**, 95 (2000).

[59] J. Ullrich, R. Moshammer, A. Dorn, R. Dörner, L. P. H. Schmidt, and H. Schmidt-Böcking, Recoil-ion and electron momentum spectroscopy: Reaction-microscopes, Rep. Prog. Phys. **66**, 1463 (2003).

[60] M. Sabbar, S. Heuser, R. Boge, M. Lucchini, L. Gallmann, C. Cirelli, and U. Keller, Combining attosecond XUV pulses with coincidence spectroscopy, Rev. Sci. Instrum. **85**, 103113 (2014).